EurJIC
European Journal of Inorganic Chemistry

A Journal of ChemPubSoc Europe

Accepted Article

Title: The synthesis of GNRs@mSiO2-ICG-DOX@Se-Se-FA nanocomposite for controlled chemo-/photothermal/ photodynamic therapy

Authors: Na An, Huiming Lin, and Fengyu Qu

To be cited as: *Eur. J. Inorg. Chem.* 10.1002/ejic.201800572

Link to VoR: http://dx.doi.org/10.1002/ejic.201800572

WILEY-VCH

10.1002/ejic.201800572

The synthesis of GNRs@mSiO$_2$-ICG-DOX@Se-Se-FA nanocomposite for controlled chemo-/photothermal/photodynamic therapy

Na An, Huiming Lin,* and Fengyu Qu*

Key Laboratory of Photochemical Biomaterials and Energy Storage Materials, Heilongjiang Province , College of Chemistry and Chemical Engineering, Harbin Normal University, Harbin, 150025, P. R. China

Tel (Fax): +86 451 88060653

E-mail: qufengyu@hrbnu.edu.cn and linhuiming@hrbnu.edu.cn

Abstract

Here, a novel core-shell nanocomposite was synthesized to integrate sensitive-chemotherapy with photodynamic therapy (PDT) and photothermal therapy (PTT) for enhanced antitumor efficiency by using gold nanorods core and mesoporous silica as shell (GNRs@$mSiO_2$) nanoparticle as host. After modified with $–NH_2$, indocyanine green (ICG, negative charge) and doxorubicin hydrochloride (DOX, positive charge) molecules could be stored in mesopores by layer-by-layer assembly method depending on the electrostatic interaction. To further inhibit the leakage, sensitive Se-Se linker was synthesized and adopted as nanovalve coated outside the nanoparticles (GNRs@$mSiO_2$-ICG-DOX@Se-Se). Under NIR (808 nm) irradiation, the heat elevation (derived from GNR/ICG) and ROS generation (derived from ICG) also can be detected in vitro. Owing to the redox sensitive of Se-Se, GNRs@$mSiO_2$-ICG-DOX@Se-Se revealed the reduction (GSH) as well as oxidation (ROS) triggered DOX release. To further make sure the specific targeting, folic acid (FA) was grafted outside due to the excess expression of FA receptor on tumor cells. The detailed cell experiments by using HepG2 as typical cancer cells showed the enhanced cytotoxicity to cancer cells owing to the synergistic effect of chemotherapy, PTT, and PDT. On account of the distinction of GSH concentration in cancer/normal cells and the on-demand operation of NIR, GNRs@$mSiO_2$-ICG-DOX@Se-Se-FA exhibited the potential application on cancer therapy.

Keywords: GNRs@$mSiO_2$; sensitive release; NIR; PDT; PTT

1 Introduction

Systematic combination of different anticancer treatments can overcome drawbacks of individual methods to improve the efficiency[1, 2, 3, 4]. With the development of nanotechnology, some nanocomposites have attracted increasing attention on nanomedicine owing to their advanced physical, chemical and biological properties[5, 6, 7, 8]. However, to integrate multicomponent into one nanoplantform to achieve the most intelligent combination for selective and synergistic therapy remains a great challenge[9, 10].

Chemotherapy is widely used for anticancer by employing cytotoxic drugs[11, 12, 13]. To improve the specific accumulation and the permeability-retention (EPR) effect, functional nanoparticles were used as the nanocarriers for targeted drug delivery to optimize chemotherapy. Besides, photothermal therapy (PTT) and photodynamic therapy (PDT) also possesses outstanding advantages on cancer treatment, such as low side effects, and remote controllability, especially avoiding chemo-resistance[14, 15, 16]. The development of PTT and PDT heavily depends on photothermal and photosensitive agents[17, 18]. Near-infrared (NIR) illumination phototherapy is ideal for real applications because of the superior tissue penetration ability[19, 20]. Up to now, many kinds of photothermal sensitizers can absorb NIR light and convert it to heat, such as gold, carbon, and grapheme oxide nanostructures[21]. Among these, gold nanorods (AuNRs) can provide a tunable and strong longitudinal surface plasmon resonance (LSPR) across the 600−1300 nm spectral range, which are considered to have great potential for combined PTT and PDT[22, 23, 24]. Yeh et al. have designed a rod-in-shell (rattle-like) Au nanostructure, which is responsive to the first (650-950 nm) and second (1000-1350 nm) NIR windows, revealing the potential application in the hyperthermia-based therapy[25]. Chen and co-workers have conjugated low-molecular-weight polyethylenimine onto the surfaces of gold nanorods with high gene transfection activity, low cytotoxicity, photoacoustic imaging ability, and photothermal therapeutic properties[26]. Choi et al. have published a gold nanorod (GNR)-photosensitizer complex for noninvasive NIR fluorescence imaging and PTT/PDT in various cancers[27].

However, the LSPR peak of AuNRs could be shifted to the visible spectral region because of their easy clustering and aggregation, resulting in a low efficiency of phototherapy in the NIR window. In order to overcome this weakness, some hard

substances were deposited on AuNRs to remain their monodispersity. Yu and co-workers have reported a AuNRs@C core−shell nanocomposites showing the favourable photothermal and biocompatibility properties under NIR light irradiation[28]. In addition, with well biocompatibility, large surface area/pore volume, tunable morphologies/functionalization, mesoporous silica is considered as one of the most potential candidates of biomaterials. The coating of mesoporous silica shell on AuNRs was also thought to be an efficient way[29]. Furthermore, the porous structure also supplies abundant space for the loading of anticancer drugs as well photosensitive agents (PS).

In this paper, a nanocomposite integrated with chemotherapy, PTT and PDT in synergistic manner, is illustrated in Scheme 1. First, -NH_2 modified AuNRs@$mSiO_2$ core-shell nanopartiles were synthesized as the host. Under layer-by-layer assembly means, PS agent (Indocyanine green, ICG) and anticancer drug (Doxorubicin hydrochloride, DOX) were loaded into the mesopore of $mSiO_2$ shell due to the electrostatic interaction. To make sure few leakages and well defined drug release, sensitive diselenide derivative was prepared and it was grafted outside the mesopore as nanovalve via a simple silane coupling reaction (Figure S1). In addition, folic acid (FA) was introduced to enhance the cancer targeting performance. When the nanocomposite (GNRs@$mSiO_2$-ICG-DOX@Se-Se-FA) was taken up by cancer cells via pinocytosis or phagocytosis, the diselenide nanovalve breaking induces DOX release owing to the high expression of GSH in cancer cell. Upon 808 nm irradiation, diselenide nanovalve which is also sensitive with ROS-trigger DOX release as well. Furthermore, the PDT and PTT causing by NIR irradiation are useful secondary cancer treatment in microenvironment. So, the PDT and PTT combines with chemotherapy would further improve the cytotoxicity to cancer cell.

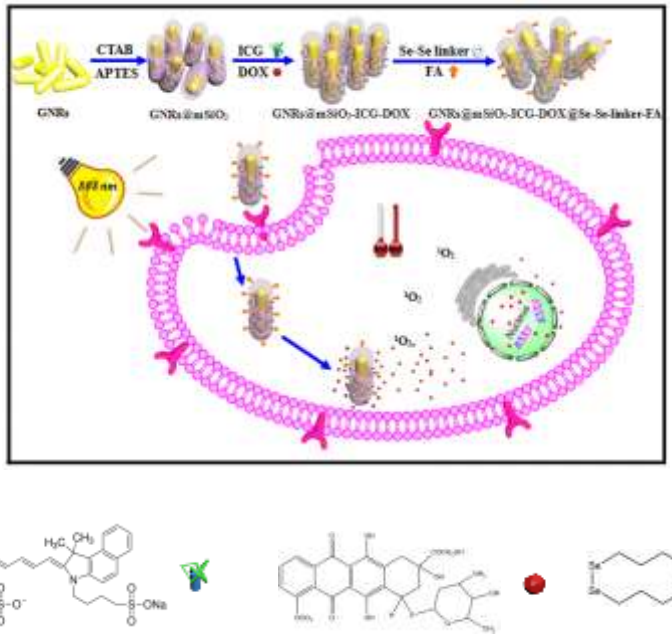

Scheme.1 Schematic illustration of the synthesis of NIR sensitive nanocomposites and the chemotherapy, PDT and PTT process.

2. Results and Discussion

2.1 Material Characterization

Transmission electron microscopy (TEM) was used to reveal the structure of the as-synthesized sample. As shown in Figure 1A, the average length and width of GNRs was 67 and 18 nm, respectively (ca. 3.7:1 aspect ratio). After the coating of $mSiO_2$, the synthesized GNRs@$mSiO_2$ possesses uniform core-shell structure with $mSiO_2$ shell about 23 nm in thickness (Figure 1B). And the worm-like mesoporous structure of the silica layer also can be found, obviously. That provides plenty of space for the loading of guest molecules. Comparing with Figure 1B, the blurred mesoporous structure as displaying in Figure 1C is ascribed to the loading of DOX/ICG and the grafting of Se-Se linker. Furthermore, the absorption spectra of the GNRs and GNRs@$mSiO_2$ were investigated (Figure 1D). Both of the two samples exhibit two absorption bands at 510 and 800 nm, corresponding to the transverse plasmon resonance and longitudinal plasmon resonance, respectively. After silica shell coating, the adsorption peak of GNRs@$mSiO_2$ shift to 817 nm, which is in accord with the related researches, due to a local increase of refractive index and the scattering from the silica shells[30]. Importantly, the longitudinal SPR peak of GNRs@$mSiO_2$ remains in the NIR region that is significant to insure the relative high transmissivity to biological tissues. Furthermore, the structure of these

nanocomposites was further revealed by XRD (Figure 1E and 1F). From Figure 1E, the diffraction peaks match well with the standard Au phase (JCPDS card no. 65-2870). Furthermore, an additional diffraction peak at about 22.2° of GNRs@mSiO$_2$ is owing to the amorphous SiO$_2$ framework. As displayed in Figure 1F, only one diffraction peak at 2.28° in LAXRD suggests the worm-like mesoporous structure of GNRs@mSiO$_2$ that also is consistent with TEM data shown in Figure 1B.

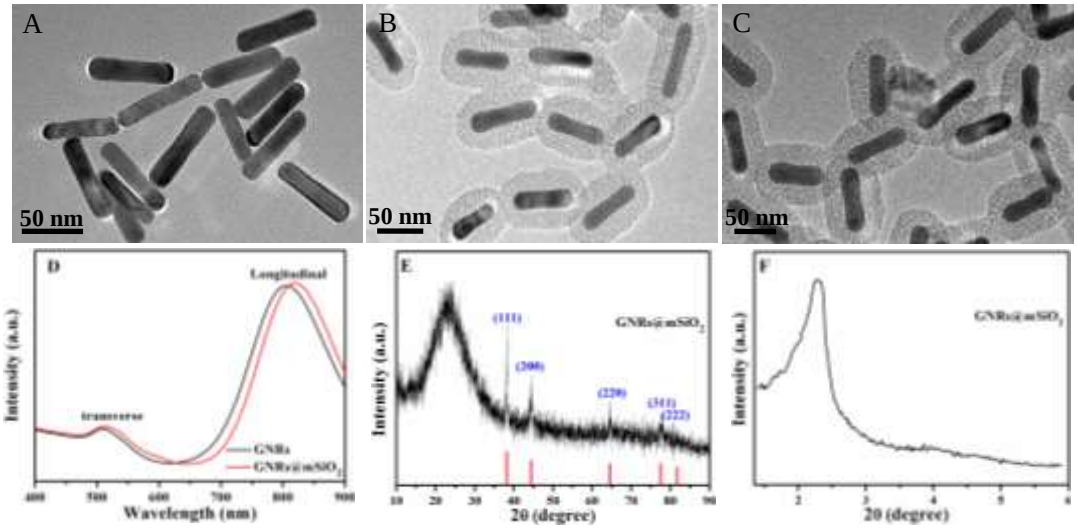

Figure 1. TEM images of (A) GNRs, (B) GNRs@mSiO$_2$, (C) GNRs@mSiO$_2$-ICG-DOX@Se-Se, (D) The UV/Vis spectrum of GNRs and GNR@mSiO$_2$, (E) Wide-angle XRD and (F) low-angle XRD patterns of GNRs@mSiO$_2$.

The mesopore silica shell supplies the plenty of room for the loading of guest molecules. To improve the loading amount, first GNRs@mSiO$_2$ was modified with –NH$_2$ groups. The successful organic modification and drug loading was also verified by FT-IR spectroscopy (Figure 2A). The wide absorption peak at 3432 cm^{-1} is ascribed to the stretching vibration of -OH from Si-OH and the absorption peak at 1089 cm^{-1}is ascribed to the Si-O-Si framework of mSiO$_2$. Figure 2(A)b, the two absorption peaks at 2919 and 2850 cm^{-1} were the symmetric and anti-symmetric vibration absorption peak caused by C-H. And the absorption peaks at 1579 (N–H in-plane deformation) and 796 cm^{-1} (N–H out-of-plane deformation) can prove the successful modification of amine group. As exhibited in Figure 2(A)c, the emerging peak at 1220 cm^{-1} ascribing to the S=O asymmetric stretching testifies the joint of ICG. From Figure 2(A)d, the absorption peaks at 1750 cm^{-1} due to the C=O functional groups of DOX. In addition, the Se-Se vibration (722 cm^{-1}) in Figure 2(A)e further confirms that Se-Se linker has been successfully introduced. Moreover, the Zeta

potentials of these composites were also detected to further reveal the modification process (Figure 2B). GNRs@$mSiO_2$ displays the negative Zeta potential (-10.99±1.62 mV) on account of the surface Si-OH with negative charge. While that increases to 8.15±1.09 mV of GNRs@$mSiO_2$-NH_2 due to the positive charge of -NH_2. With sulfonate group, ICG (negative charge) can be connected onto GNRs@$mSiO_2$-NH_2 owing to the electrostatic interaction, inducing the negative charge of GNRs@$mSiO_2$-ICG (-1.45±1.08 mV). And the negative surface of GNRs@$mSiO_2$-ICG also provides the site for the further loading of DOX molecules with positive charge. The increasing Zeta potential of GNRs@$mSiO_2$-ICG-DOX (3.76±1.61 mV) and GNRs@$mSiO_2$-ICG-DOX@Se-Se (5.70±0.81 mV) further testifies the DOX loading and Se-Se linker modification. So, the amount of –NH_2 graft also can influence the ICG as well as DOX loading amount (Table S1). In addition, the UV/Vis absorption spectra of these materials were investigated (Figure 2C). Comparing with GNRs@$mSiO_2$, the emerging absorption peak at 483 and 737 nm of GNRs@$mSiO_2$-ICG-DOX@Se-Se is derived from the typical adsorption of DOX and ICG, respectively.

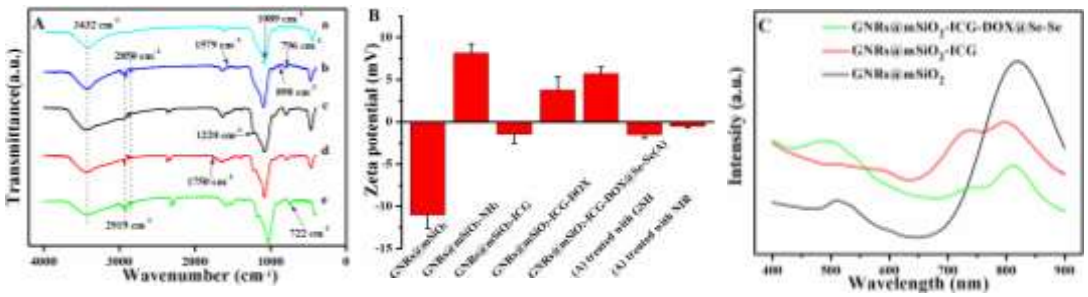

Figure 2.(A) FTIR spectra of (a) GNRs@$mSiO_2$, (b) GNRs@$mSiO_2$-NH_2, (c) GNRs@$mSiO_2$-ICG, (d) GNRs@$mSiO_2$-ICG-DOX and (e)GNRs@$mSiO_2$-ICG-DOX@Se-Se, (B) Zeta potentials and (C) the UV/Vis spectrum of these samples.

To investigate the porous structure of the nanocomposite, N_2 adsorption-desorption isotherms of GNRs@$mSiO_2$ and GNRs@$mSiO_2$-ICG-DOX@Se-Se2 were carried out (Figure 3). The typical IV isotherm curves reveal the mesoporous structure of $mSiO_2$ shell. And the hysteresis loop at high P/P_0 region is ascribed to the void derived from the accumulation of these small nanoparticles. Moreover, after the organic modification and drug loading, the corresponding surface area and pore volume reduces from 531.87 $m^2\ g^{-1}$, and 0.51 $cm^3\ g^{-1}$ to 402.15 $m^2\ g^{-1}$ and 0.23 $cm^3\ g^{-1}$ (Table S2).

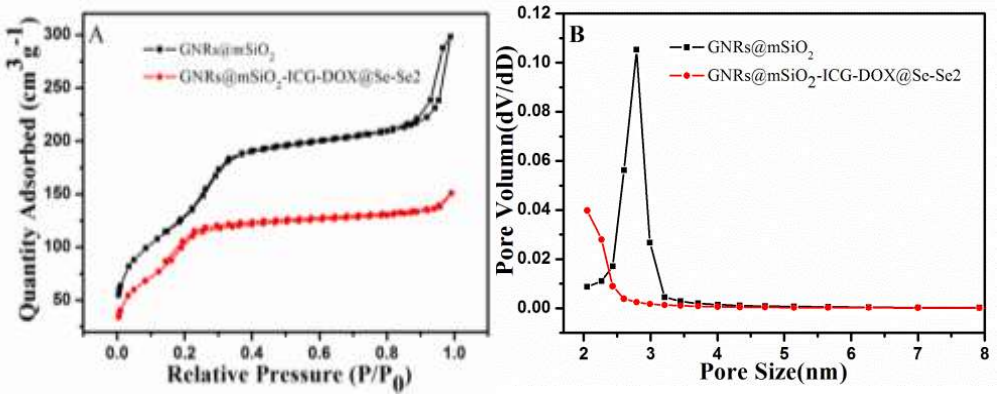

Figure 3. (A) Nitrogen adsorption–desorption isotherms and (B) pore size distribution curves of these samples.

2.2 Photothermal and photodynamic properties

The temperature of GNRs@$mSiO_2$ and GNRs@$mSiO_2$-ICG2 suspension solution under laser irradiation (808 nm, 2 W cm^{-2}) was monitored to evaluate the photothermal efficiency. As shown in Figure 4A, when 808 nm NIR is introduced, the temperature increases obviously, and all the samples show the time-dependent temperature increase. Under illuminating for 14 min, GNRs@$mSiO_2$ reaches 47.3 ℃. After loading of ICG, the temperature of GNRs@$mSiO_2$-ICG2 further rises to 49.5 ℃. Meanwhile, pure water just shows 31.2 ℃ under the same condition. Based on Figure 4A, it is believed that the rapid temperature rise of GNRs@$mSiO_2$ and GNRs@$mSiO_2$-ICG2 is ascribed to GNRs and ICG, which are typical photothermal agents. Then temperature increasing test under different laser irradiation intensity (1, 2 and 3 W cm^{-2}) of GNRs@$mSiO_2$-ICG2 was carried out (Figure 4B). The maximal temperature of GNRs@$mSiO_2$-ICG2 increases to 45.0, 47.3 and 49.5℃ under 1, 2 and 3 W cm^{-2} irradiation, respectively. The photothermal conversion efficiency (η) is calculated according to formula (1) .

$$\eta = \frac{hA(T_{max} - T_s) - Q_0}{I(1 - 10^{-A\lambda})} \quad (1)$$

Calculated from the Figure 4C and D, photothermal conversion coefficient (η) of GNRs@$mSiO_2$-ICG2 is about 23.8 %. From the above result, the as-synthesized GNRs@$mSiO_2$-ICG2 exhibits the remarkable time/intensity-dependent temperature elevation that is significant for the controlled photothermal therapy in practical application.

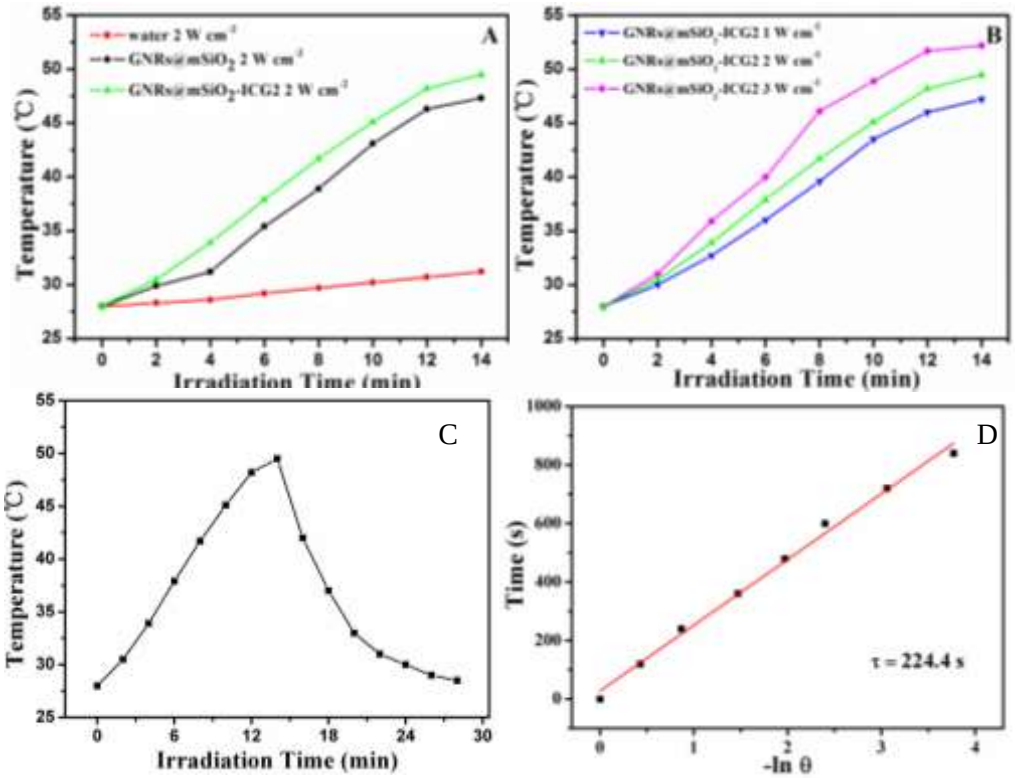

Figure 4. (A) Temperature elevation of water and aqueous dispersion of GNRs@$mSiO_2$ and GNRs@$mSiO_2$-ICG under 2 W cm^{-2} 808 nm irradiation, (B) Temperature elevation of aqueous dispersion of GNRs@$mSiO_2$-ICG2 with different power density (1, 2 and 3 W cm^{-2}) as a function of irradiation time. (C) Temperature evolution of the dispersion of GNRs@$mSiO_2$-ICG2 during heating (laser on) and cooling (laser off). (D) Thermal equilibrium time constant of the four systems determined by fitting the time data versus negative natural logarithm of the driving force temperature from the cooling period. Sample concentration is 0.5 mg mL^{-1}.

As we all known, ICG molecules can absorb NIR to reach the high vibration energy level of excited state. Then it does not only generate thermal energy but also ROS during the deactivation process. The $^1O_2$ generation of GNRs@$mSiO_2$-ICG NPs upon 808 nm irradiation was assessed by monitoring the photo degradation of diphenylisobenzofuran (DPBF), which is a widely used singlet oxygen detector. Figure 5A shows the UV/Vis spectra of DPBF cultured with GNRs@$mSiO_2$-ICG2 after 808 nm NIR irradiation (2 W cm^{-2}) for 0-80 min. From Figure 5A, the typical absorption of DPBF significantly decreases with 808 nm irradiation, implying the efficient generation of $^1O_2$ from GNRs@$mSiO_2$-ICG. In addition, the decay curves of DPBF absorbance at 407 nm incubated with different samples as a function of irradiation time was summarized in Figure 5B. GNRs@$mSiO_2$ does not give notable degradation of DPBF even on exposure to 808 nm NIR for 80 min, whereas

GNRs@mSiO$_2$-ICG shows a clear degradation of DPBF. Increasing the loading amount of ICG, the sample reveals enhanced degradation activation as well as increased $^1O_2$ generation. With most amount of ICG, GNRs@mSiO$_2$-ICG2 possess the most generation of $^1O_2$. The above results indicated that GNRs@mSiO$_2$-ICG NPs could be used as a photothermal and photodynamic agent for simultaneous PDT/PTT therapy triggered by single 808 nm laser.

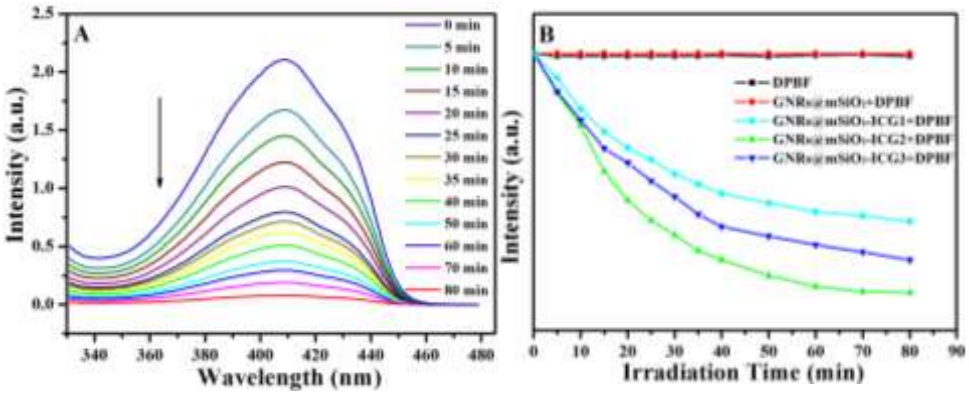

Figure 5. (A) UV/Vis spectra of DPBF after irradiation of GNRs@mSiO$_2$-ICG2 with 808 nm NIR (2 W cm^{-2}) for 0 to 80 min and (B) the decay curves of DPBF absorbance at 407 nm in different solutions as a function of irradiation time.

2.3. Drug release profiles

To further insure the triggered release behaviors of these nanocomposites, sensitive Se-Se linker was synthesized to encapsulate drug molecules in the mesopore and the corresponding controlled release was investigated as shown in Figure 6. From Figure 6A, all the samples display the GSH triggered DOX release, distinctly. In the absence of GSH, GNRs@mSiO$_2$-ICG-DOX@Se-Se1, GNRs@mSiO$_2$-ICG-DOX@Se-Se2 and GNRs@mSiO$_2$-ICG-DOX@Se-Se3 all show the low release rate with few release amounts below 14.15 % within 48 h. With GSH in the media, the release rates were enhanced remarkably and the release amount of DOX can reach as high as 85.13 %, 80.03 % and 73.77 % for GNRs@mSiO$_2$-ICG-DOX@Se-Se1, GNRs@mSiO$_2$-ICG-DOX@Se-Se2 and GNRs@mSiO$_2$-ICG-DOX@Se-Se3, respectively. In addition, the amount of Se-Se linker also influences the release performance. As exhibited in Figure 6A, with the least amount of Se-Se linker, GNRs@mSiO$_2$-ICG-DOX@Se-Se1 possesses the highest DOX release up to 85.13 % (with GSH), while the most DOX leak about 14.15 % (without GSH) also can be found from GNRs@mSiO$_2$-ICG-DOX@Se-Se1 due to the insufficient Se-Se linker.

However, too much Se-Se linker also is not insufficiency owing to its low drug release (73.77 % of GNRs@mSiO$_2$-ICG-DOX@Se-Se3) even with GSH. Here, GNRs@mSiO$_2$-ICG-DOX@Se-Se2 was thought to be the appropriate one to reveal the low leak without GSH and the high release amount with GSH. Moreover, the effect of GSH concentration on the DOX release was also investigated by varying 5, 10, and 20 mM of GSH in media. From Figure 6B, 5 mM of GSH induces 62.99 % DOX release at 24 h, and that aggrandizes to 83.03 % and 91.00 % with the increase of GSH to 10 and 20 mM, respectively. The GSH concentration-dependent drug release as shown in Figure 6B further confirms the GSH-sensitive DOX release behavior of GNRs@mSiO$_2$-ICG-DOX@Se-Se. From Figure 2B, the Zeta potential of GNRs@mSiO$_2$-ICG-DOX@Se-Se treated with GSH drops to -1.52 mV, due to the fact that the sensitive Se-Se bond can be broken by some reducing agents, including GSH, to form –Se-H group with negative charge. In view of the above investigation, it is believed that the sensitive release behavior is owing to the Se-Se linkers. They were used as nanovalves and modified outside mesopore to inhibit drug leak. With GSH, the Se-Se linker was cleaved to induce nanovalves open and drug release. That is significant for the specific drug release to tumor fractions with high concentration of GSH and low leak in normal tissue (low concentration of GSH).

Figure 6C shows the release profiles of GNRs@mSiO$_2$-ICG-DOX@Se-Se2 under different light irradiation intensities. To avoid the photothermal effect, the irradiation was introduced 2 min every half an hour and without any insulation measure. In compared with the dark condition, 808 nm NIR light accelerates the release rate. By increasing the irradiation times, the release amount increases as well. It takes 2 h (with irradiation for 8 min) for GNRs@mSiO$_2$-ICG-DOX@Se-Se2 to reach 6.02 % release, and after 8 h (with irradiation for 32 min) the release raise to 25.31 % (1 W cm^{-2}). Further elevating the irradiation intensity, the release can be enhanced to 33.31 % (2 W cm^{-2}) and 37.75 % (3 W cm^{-2}). It is known that Se-Se bond is cleavable not only by reducing agents, but also by oxidizing agent. Based on the above investigation in Figure 5, NIR simulates GNRs@mSiO$_2$-ICG to induce ROS generation, which could disrupt Se-Se linker and cause drug release. In addition, the broken of Se-Se bond under NIR was also monitored by Zeta potential. From Figure 2B, Zeta potential of GNRs@mSiO$_2$-ICG-DOX@Se-Se2 treated by NIR decreases from 5.70±0.81 to -0.52±0.20 mV, because the oxidization of Se-Se bond leaves

–Se-OOH at the surface. In addition, the release performance with continuous NIR irradiation was carried out. From Figure 6D, when 808 nm NIR was introduced for 10 min, 22.19 % DOX release can be detected. Prolonging the illumination to 20 and 30 min, the release aggrandizes to 30.54 % and 47.92 %, respectively. Further extending the irradiation to 40 min, the release increases slowly to 50.36 %, tending to its equilibrium.

To further study the release performance of GNRs@mSiO$_2$-ICG-DOX@Se-Se2 under different conditions, Higuchi model was used to treat these release data. As we known, drug release kinetics from an insoluble porous carrier matrix are frequently described by the Higuchi model, and the release rate could be described by the equation (2):

$$Q = kt^{1/2} \qquad (2)$$

in which Q denotes the amount of drug released from the materials, t is time, and *k* is the Higuchi dissolution constant. According to the model, for a purely diffusion-controlled process, the linear relationship is valid for the release of relatively small molecules distributed uniformly throughout the carrier. As shown in Figure 6E, without GSH and irradiation, dissolution constant k equals to 1.69. That increases remarkably to 14.31, 23.39 and 35.26 with addition of GSH to 5, 10 and 20 mM, owing to GSH-triggered Se-Se linker broken and drug release. And the higher concentration of GSH can induce the faster linker disruption as well as the higher dissolution constant. The pulsing irradiation also induces the dissolution constant rise to 10.78-16.32. Increasing the irradiation intensity to 3W cm^{-2}, *k* grows to 16.32, due to more ROS generation. By comparing the release performances, GSH makes the higher *k* and release amount than that of illumination. From Figure 2B, GNRs@mSiO$_2$-ICG-DOX@Se-Se treated by GSH (-1.52 mV) possesses the lower Zeta potential than that of the treated by 808 nm NIR (-0.52 mV). This means that under these conditions, GSH is more effective to induce the bond broken than illumination (ROS generation). In addition, the continuous 808 nm illumination leads to the highest dissolution constant of all (*k*=63.60). The continuous 808 nm illumination causes not only ROS generation but also photothermal effect, which can accelerate the diffusion of DOX out. Even so, the release amount (50.36 %) is also less than that of GSH (62.90-91.00 %).

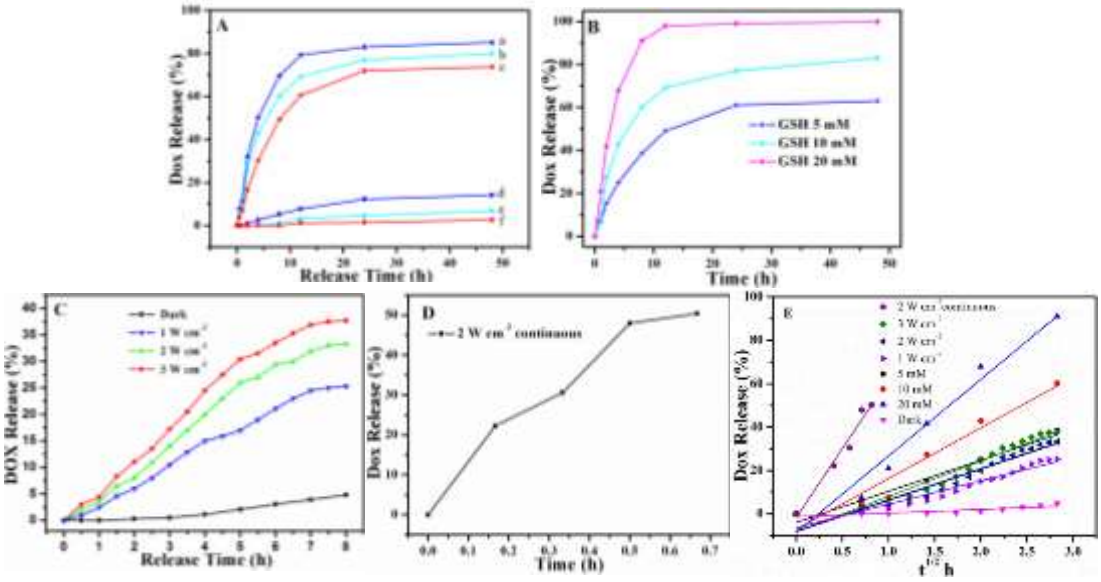

Figure 6. (A) Release profiles of GNRs@mSiO$_2$-ICG-DOX@Se-Se1(a, d), GNRs@mSiO$_2$-ICG-DOX@Se-Se2(b, e) and GNRs@mSiO$_2$-ICG-DOX@Se-Se3(c, f) with (a-c) and without (d-f) 10 mM of GSH, (B) Release profiles of GNRs@mSiO$_2$-ICG-DOX@Se-Se2 with different concentration of GSH, (C) Release profiles ofGNRs@mSiO$_2$-ICG-DOX@Se-Se2 under vary irradiation intensities (every 30 min with irradiation for 2min), (D) Release profiles of GNRs@mSiO$_2$-ICG-DOX@Se-Se2 with continues illumination, (E) Release Higuchi plot of DOX released with different release conditions.

2.4 Cell experiments

In order to observe the uptake and subsequent localization of GNRs@mSiO$_2$-ICG-DOX@Se-Se2-FA, the nanocomposites (500 μg mL^{-1}) were pre-incubated with the HepG2 cells for 1, 3 and 6 h in the dark and then 808 nm irradiation for 20 min. As can be seen from Figure 7, the red (DOX, 480 nm) emission can be found in cytoplasm, implying these nanocomposites have been internalized by HepG2 cells through endocytosis or macropinocytosis owing to nano-size particles and -FA targeting. Furthermore, with extending the incubated time, the red fluorescence emission is enhanced, ascribing to the time-dependent uptake of GNRs@mSiO$_2$-ICG-DOX@Se-Se2-FA into HepG2. Under 808 nm illuminating, more red-fluorescence emission emerges in cell nucleus, indicating a continuous released DOX molecules gathering into nucleus to improve the chemotherapy.

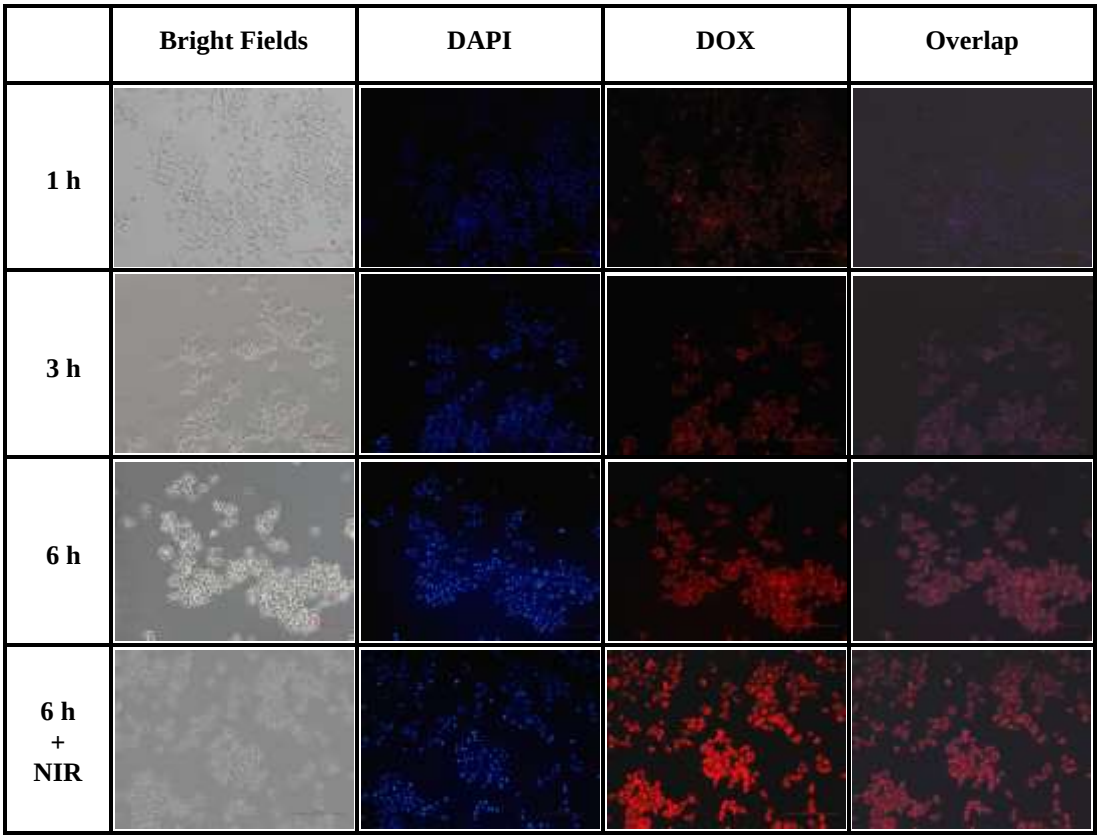

Figure 7.Colocalization fluorescent images recorded for HepG2 cells after incubation with GNRs@mSiO$_2$-ICG-DOX@Se-Se2-FA (500 μg mL^{-1}) for 1, 3, 6 h and 6 h with 808 nm NIR.

ROS are generally short-lived molecules and can oxidize plenty of macromolecules, such as DNA and proteins, which stimulates inflammation and initiates pro-apoptotic cellular signaling, resulting in the irreversible cell damage. So the level of intracellular ROS has a great effect on PDT. Here, the intracellular ROS generation of HepG2 cells incubated with GNRs@mSiO$_2$-ICG-FA was surveyed by using DCFH-DA as an indicator, which is oxidized to form, 2'7'-dichlofluorescein, a green fluorescent substance inside cells. As shown in Figure 8, strong green fluorescence is observed in HepG2 co-cultured with GNRs@mSiO$_2$-ICG-FAunder 808 nm irradiation. However, without NIR irradiation or GNRs@mSiO$_2$-ICG-FA, there is not remarked green fluorescence in cells. From Figure 8, the intracellular ROS generation induces GNRs@mSiO$_2$-ICG-FA can be adopted as PDT agent. And the visualized change of cell survival incubated GNRs@mSiO$_2$-ICG-FAwith 808 nm irradiation was also recorded by using Calcein AM as living cells dye (Figure S4). The decrease green fluorescence is ascribed to NIR light-triggered cytotoxicity, derived from intracellular heat and ROS generation.

10.1002/ejic.201800572

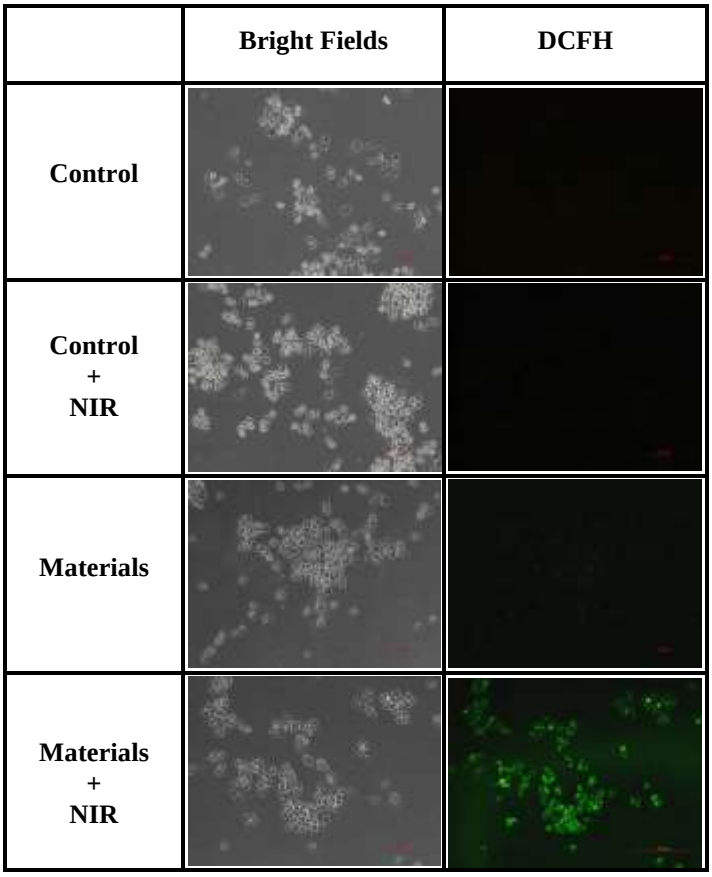

Figure 8.Bright-field and fluorescence images of HepG2 cells after the co-incubation with GNRs@mSiO$_2$-ICG-FA for 12 h. First row: no GNRs@mSiO$_2$-ICG-FA no NIR light, Second row: no GNRs@mSiO$_2$-ICG-FA, with NIR light, Third row: GNRs@mSiO$_2$-ICG-FA, no NIR light, Fourth row: GNRs@mSiO$_2$-ICG-FA and NIR light irradiation (500 μg mL^{-1}, 808 nm, 2 W cm^{-2}, 20 min).

Besides, MTT assay was carried out to further quantificationally analyze the cytotoxicity of these nanocomposites. The viabilities of HepG2 cells incubated with different concentrations of GNRs@mSiO$_2$-FA, GNRs@mSiO$_2$-ICG-FA, GNRs@mSiO$_2$-ICG-DOX@Se-Se-FA and GNRs@mSiO$_2$-ICG-DOX@Se-Se-FA with NIR irradiation (2 W cm^{-2}) were summarized in Figure 9. From Figure 9, GNRs@mSiO$_2$-FA and GNRs@mSiO$_2$-ICG-FA do not show obvious toxicity towards to HepG2 cells. Even when the concentration rises to 125 μg mL^{-1}, the cell survival rate remains at 82.67±1.44% and 81.44±1.32%, respectively. GNRs@mSiO$_2$-ICG-DOX@Se-Se-FA displays the significant concentration-dependent cell viability. With the increase concentration to 125 μg mL^{-1}, the cell viability drops to 53.44±2.44%, owing to the intracellular GSH-triggered

DOX release. When 808 nm NIR is introduced, the cell viability further decreases to 34.21±1.90 % (125 μg mL^{-1}). The decreased cell viability is mainly attributing to the combination effect of chemotherapy and PDT/PTT as above investigation. It is known that the HeLa cell (cervical cancer cell line) possesses high expression of FA-receptor and cell experiment of HeLa cell treated by GNRs@$mSiO_2$-ICG-DOX@Se-Se-FA was also carried out as contrast. And the lower cell viability toward HeLa cell (32.17±2.30 %) than that in HepG2 (34.21±1.90 %) is ascribed to the FA targeting.

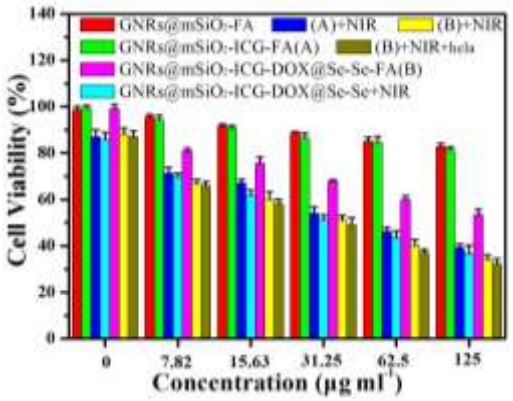

Figure 9. Viability of HepG2 and HeLa cells incubated with different concentration of nanocomposites with and without NIR irradiation (808 nm, 2 Wcm^{-2} for 20 min).

3 Conclusions

In this chapter, the NIR sensitive GNRs@$mSiO_2$ core-shell nanopartiles were prepared as host. $mSiO_2$ shell not only remained the monodispersity of GNRs but also supplied plenty of space for drug storage. By adjusting the surface charge, photosensitizer ICG and anti-cancer drug DOX can be loaded in the mesopore in succession depending on the electrostatic interaction. Here, redox response Se-Se linkers were synthesized to block the orifice and to inhibit drug leakage. The nanocomposite displayed the GSH-dependent DOX release. Moreover, under NIR irradiation, the ROS generation also can degrade Se-Se nanovalves to induce DOX release. Under the investigation of the release kinetics, reduction is more efficient to induce Se-Se linker broken than oxidation. In addition, the detailed cell experiments by using HepG2 as typical cancer cells further showed the improved cytotoxicity owing to the fast uptake, specific chemotherapy and PTT/PDT. These novel

advantages also make GNRs@mSiO$_2$-ICG-DOX@Se-Se-FA as a potential candidate agent for targeted anticancer.

4 Experimental sections

4.1 Materials

All of the chemicals were analytical grade and were used without further purification. chloroauric acid ($HAuCl_4{\cdot}3H_2O$), silver nitrate ($AgNO_3$), hexadecyltrimethyl ammonium bromide (CTAB), tetraethyl orthosilicate (TEOS), selenium powder, sodium borohydride ($NaBH_4$), 3-bromo-1-propanol, 3-(triethoxysilyl) propyl isocyanate, doxorubicin hydrochloride (DOX), glutathione (reduced), N-(3-Dimethylaminopropyl)-N'-ethylcarbodiimide hydrochloride (EDC), ascorbic acid, (3-aminopropyl)triethoxysilane(APTES), N-Hydroxysuccinimide (NHS), and folic acid (FA), were obtained from Aladdin, China. 3-[4,5-dimethylthialzol-2-yl]-2,5-diphenyltetrazolium bromide (MTT) and 1-octadecene were purchased from Sigma-Aldrich. Dimethyl sulfoxide (DMSO), hexahydrate, ethanol, n-hexane, dichloromethane, ethyl acetate and tetrahydrofuran (THF) were purchased from Tianjin Chemical Corp. of China.

4.2 Instruments

Samples were characterized by transmission electron microscopy (TEM Hitachi H-8100) at an accelerating voltage of 20 kV. X-ray diffraction (XRD) date is characterized using a Siemens D5005diffractometer with Cu Ka radiation at 40 kV and 30 mA. A Fourier transform infrared (FT-IR) spectroscopy spectrometer (JASCOFT/IR-420) was used to record the infrared spectra of all samples. Zeta potential was carried out on the Brookhaven. Ultraviolet-visible (UV-Vis) spectra were taken on a SHIMADZU UV-2550 spectrophotometer. The isotherms of N_2 adsorption/desorption were measured at the temperature of liquid nitrogen using a Micromeritics ASAP 2010M system. The pore size distributions were calculated from the N_2 adsorption isotherms using the Barrett-Joyner-Halenda model. The fluorescence imaging experiments were carried out on the Leica DFC450C Microsystems Ltd. using a 10 × objective.

4.3 Synthetic procedures

Synthesis of GNRs： GNRs was synthesized by seed-mediated growth by following procedures described by Jana and Nikoobakht[31]. CTAB solution (0.20 M, 5 mL) was mixed with $HAuCl_4$ solution (0.5 mM, 5 mL), then ice-cold $NaBH_4$ solution (0.01 M, 0.60 mL) was added and the mixture was stirred vigorously for 2 min at 25℃ (formation of a brownish yellow seed solution). The growth solution was made by adding $AgNO_3$ (4 mM, 0.25 mL) and then $HAuCl_4$ (1 mM, 5 mL) to CTAB solution (0.20 M, 5 mL), under gentle mixing, followed by the addition of ascorbic acid solution (0.0788 M, 70 μL). To grow nanorods, the seed solution (12 μL) was added to the growth solution at 27–30℃. The color of the solution changed to burgundy within 10–20 min. The solution was then centrifuged at 12000 rpm for 15 min, and the collected CTAB gold nanorods were redispersed in deionized water.

Synthesis of GNRs@mSiO$_2$： The as-synthesized gold nanorods were dispersed in deionized water (10 mL), then 0.1 M NaOH solution was added (pH adjusted to 10) with vigorous stirring. Three 30 μL injections of 20% TEOS in ethanol were added under gentle stirring at 30 min intervals. The mixture was stirred for 48 h at 32 ℃, and the obtained mesoporous silica coated gold nanorods were collected and washed several times with ethanol to remove the unreacted species. At last, the collected products were refluxing in methanol (1wt% NaCl) for 3 h at room temperature to remove the template CTAB.

Synthesis of Diselenide linker (Se-Se linker)： Selenium powder (6.3 mM) was added to 25 mL of water containing dissolved $NaBH_4$ (13.2 mM) with magnetic stirring in the ice bath. After the initial vigorous reaction had subsided (10 min), an additional selenium powder (6.3 mM) was added. The mixture was stirred for 15 min and then warmed in a steam bath to complete the dissolution of the selenium. A brownish red aqueous solution of Na_2Se_2 was obtained[32, 33, 34].

The Na_2Se_2 solution was removed to a 100 mL flask, which was sealed with a rubber plug, and then a solution of 1.7513g (12.6 mM) 3-bromo-1-propanol in 20 mL of anhydrous THF was injected into it under N_2 flow. The reaction was performed at 50 ℃ for 6 h and the obtained solution was extracted three times with 20 mL of CH_2Cl_2 and dried with anhydrous Na_2SO_4. The product was then purified by column

chromatography with a 1:1 mixture of CH_2Cl_2 and ethyl acetate as the eluent. A yellow transparent liquid was obtained with a yield of 45% (HO-Se-Se-OH). ^{1}HNMR (200 MHz) δ3.78 (t, J=6.2 Hz, 4 H), 3.04 (t, J= 7.2 Hz, 4 H), 2.02 (quintet, J= 6.6 Hz, 4 H), 1.68 (br s, 2 H).

(1.35 mM) HO-Se-Se-OH was dissolved in 5 mL of anhydrous THF in a 20 mL flask and sealed with a rubber plug. The flask was then degassed by Ar for 20 min. 3-(triethoxysilyl) propyl isocyanate (1.49 mM) in 2 mL anhydrous THF was injected into the flask under Ar flow. The system was transferred into an oil bath at 50 ℃ to react for 12 h with stirring.

Synthesis of GNRs@mSiO$_2$-ICG-DOX@Se-Se： First, 30 mg of GNRs@SiO_2 was added to 8 mL of anhydrous methanol and stirred for 10 min before adding of APTES (10, 20 and 30 μL), then stirring at room temperature for 12 h. The nanoparticles were collected by centrifugation, washed three times with methanol to obtain GNRs@mSiO$_2$-NH_2. And then, the above sample and 3 mg of ICG were added to 8 mL of anhydrous methanol and stirred for 12 h (The obtained samples are named as GNRs@SiO_2-ICG1, GNRs@SiO_2-ICG2 and GNRs@SiO_2-ICG3, respectively). Later, DOX (8 mg) was added and stirring for another 12 h. Finally, Se-Se linker (5, 10 and 15 μL) was dropwised to the mixed solution. The obtained solids (named as GNRs@SiO_2-ICG-DOX@Se-Se1, GNRs@SiO_2-ICG-DOX@Se-Se2, GNRs@SiO_2-ICG-DOX@Se-Se3, respectively) were centrifuged, washed several times with methanol solution and dried for backup. The amount of DOX and ICG loading was estimated by UV-Vis spectroscopy at 480 and 783 nm. The loading ratio (LR wt %) was ascertained by using the formula (3) and (4). The experiments were repeated three times.

$$\text{LR wt\%} = \frac{m_{(\text{initial DOX})} - m_{(\text{residual DOX})}}{m_{(\text{total sample})}} \times 100\% \qquad (3)$$

$$\text{LR wt\%} = \frac{m_{(\text{initial ICG})} - m_{(\text{residual ICG})}}{m_{(\text{total sample})}} \times 100\% \qquad (4)$$

Synthesis of FA-Modified GNRs@mSiO$_2$-ICG-DOX@Se-Se： In a typical reaction, folic acid (441.4 mg), EDC (191.7 mg), NHS (115.1 mg) and APTES (442.7 mg)

were added to DMSO (2 mL). The reaction mixture was reacted for 24 h with stirring at room temperature. The as-synthesized FA-APTES (100 μL) and GNRs@SiO_2-ICG-DOX@Se-Se (60 mg) were added to methanol (5 mL), and the reaction mixture was stirred for 24 h. The product was washed twice with methanol to remove any unreacted species.

In vitro drug release： To evaluate the drug release properties, the dried GNRs@SiO_2-ICG-DOX@Se-Se nanoparticles were exposed to PBS of pH 6.5 with 10 mM GSH or not. Then the in vitro drug release was performed at 37 ℃. The solution was taken out to determine the release amount by UV-Vis at different time intervals. The cumulative drug release was calculated according to the following formula (5):

$$\text{Cumulative drug release}(\%) = {}^{m_t}/_{m} \times 100\% \quad (5)$$

Where m_t is the amount of DOX released at time t and m is the total DOX amount loaded in the nanoparticles.

Photothermal： A volume of 2 mL of sample solution (0.5 mg mL^{-1}) was added to cuvette and irradiated with 808 nm laser (1, 2 and 3 W cm^{-2}) and the temperature was recorded every 2 min with Fluke 59 infrared thermometer.

Extracellular singlet oxygen detection： The generation of singlet oxygen was measured by using DPBF as probe. In a typical process, 1 mg of GNRs@SiO_2-ICG was dispersed well in 2 mL of DPBF solution (0.5 mg mL^{-1}) with stirring in the dark. Then the mixture was irradiated with 808 nm NIR laser for various time periods. The generation of singlet oxygen was demonstrated by the characteristic absorbance of the DPBF using a UV-Vis absorption spectrum.

Cell culture: HepG2 cells (human hepatoma cells) were incubated in monolayer in Dulbecco's Modified Eagle's Medium (DMEM, Hyclone) supplemented with 10% (v/v) fetal bovine serum (FBS, Gibco) with 100 U $mL^{-1}$of penicillin and 100 mg mL^{-1} of streptomycin under a humidified atmosphere at 37 ℃ with 5 % CO_2.

Fluorescence imaging: To analyze the ability of cellular internalization, HepG2 cells were cultured in a 6-well plates with the incubation medium (DMEM) for 24 h. GNRs@SiO_2-ICG-DOX@Se-Se2 was added into the incubation medium at the concentration of 500 μg mL^{-1} with the same cell culture condition. After incubation for 6 h, the medium was removed and the cell was washed twice with PBS (pH = 7.4), then the fluorescence imaging experiments were carried out on the Leica DFC450 C Microsystems Ltd. using a 10× objective.

Vitro cell assay: HepG2 cells were used to carry out for MTT test. The cell viability after treated with the nanoparticles was investigated using MTT assay. The assay was carried out in five times with the same manner. For the MTT assay, 1×10^4/well HepG2 cells were seeded into 96-well plates in 100 μL of media and grown for 24 h to allow cell attachment. Then the cells were incubated with samples under different concentrations for 24 h. Afterwards, 20 μL of MTT (5 mg mL^{-1}) solution were added to the incubation media for 4 h in dark. Upon the removal of MTT solution, the precipitated formazan violet crystals generated by live cells were dissolved in 150 μL of dimethyl sulfoxide (DMSO). The absorbance was quantified by a microplate reader (Bio-TekELx800) with the wavelength of 492 nm. The cytotoxicity was expressed as the percentage of cell viability compared to untreated cells. The cell viability was calculated as follows:

$$\text{Cell viability}(\%) = {I_{\text{sample}}}/{I_{\text{untreated}}} \times 100\% \qquad (6)$$

Acknowledgements

This work was supported by the National Natural Science Foundation of China (21471041, 21571045), and College Youth Innovation Talents Training Program of Heilongjiang Province of China UNPYSCT-2015053.

Supporting information (see footnote on the first page of this article): The synthetic approach of the as-synthesized Se-Se linker; drug loading; additional results and analyses of TEM images, UV-Vis spectra, release curves and fluorescence images.

References

[1] Zheng, M.; Yue, C.; Ma, Y.; Gong, P.; Zhao, P.; Zheng, C.; Sheng, Z.; Zhang, P.; Wang, Z.; Cai, L. Single-Step Assembly of DOX/ICG Loaded Lipid–Polymer Nanoparticles for Highly Effective Chemo-photothermal Combination Therapy. *ACS Nano* **2013,** *7* (3), 2056-2067.

[2]Sun, M.; Peng, D.; Hao, H.; Hu, J.; Wang, D.; Wang, K.; Liu, J.; Guo, X.; Wei, Y.; Gao, W. Thermally Triggered in Situ Assembly of Gold Nanoparticles for Cancer Multimodal Imaging and Photothermal Therapy. *ACS Appl. Mater. Interfaces.* **2017,** *9* (12), 10453-10460.

[3] Monaco, I.; Arena, F.; Biffi, S.; Locatelli, E.; Bortot, B.; La Cava, F.; Marini, G. M.; Severini, G. M.; Terreno, E.; Comes Franchini, M. Synthesis of Lipophilic Core–Shell Fe_3O_4@SiO_2@Au Nanoparticles and Polymeric Entrapment into Nanomicelles: A Novel Nanosystem for in Vivo Active Targeting and Magnetic Resonance–Photoacoustic Dual Imaging. *Bioconjugate Chem.* **2017,** *28* (5), 1382-1390.

[4] Guo, W.; Guo, C.; Zheng, N.; Sun, T.; Liu, S. $CsxWO_3$ Nanorods Coated with Polyelectrolyte Multilayers as a Multifunctional Nanomaterial for Bimodal Imaging‐Guided Photothermal/Photodynamic Cancer Treatment. *Adv. Mater.* **2016,** *29* (4), 1604157.

[5] Li, J.; Liu, J.; Chen, C. Remote Control and Modulation of Cellular Events by Plasmonic Gold Nanoparticles: Implications and Opportunities for Biomedical Applications. *ACS Nano* **2017,** *11* (3), 2403-2409.

[6]Karimi, M.; Sahandi Zangabad, P.; Baghaee-Ravari, S.; Ghazadeh, M.; Mirshekari, H.; Hamblin, M. R. Smart Nanostructures for Cargo Delivery: Uncaging and Activating by Light. *J. Am. Chem. Soc.* **2017,** *139* (13), 4584-4610.

[7] Janković, V.; Yang, Y.; You, J.; Dou, L.; Liu, Y.; Cheung, P.; Chang, J. P.; Yang, Y. Active Layer-Incorporated, Spectrally Tuned Au/SiO_2 Core/Shell Nanorod-Based Light Trapping for Organic Photovoltaics. *ACS Nano* **2013,** *7* (5), 3815-3822.

[8] Han, K.; Zhang, J.; Zhang, W.; Wang, S.; Xu, L.; Zhang, C.; Zhang, X.; Han, H. Tumor-Triggered Geometrical Shape Switch of Chimeric Peptide for Enhanced in Vivo Tumor Internalization and Photodynamic Therapy. *ACS Nano* **2017,** *11* (3), 3178-3188.

[9] Guan, T.; Shang, W.; Li, H.; Yang, X.; Fang, C.; Tian, J.; Wang, K. From Detection to Resection: Photoacoustic Tomography and Surgery Guidance with Indocyanine Green Loaded Gold Nanorod@liposome Core–Shell Nanoparticles in Liver Cancer. *Bioconjugate Chem.* **2017,** *28* (4), 1221-1228.

[10] Cheng, S. H.; Lee, C. H.; Yang, C.-S.; Tseng, F. G.; Mou, C. Y.; Lo, L. W. Mesoporous silica nanoparticles functionalized with an oxygen-sensing probe for cell photodynamic therapy: potential cancer theranostics. *J. Mater. Chem.* **2009,** *19* (9), 1252-1257.

[11] Liu, B.; Li, C.; Cheng, Z.; Hou, Z.; Huang, S.; Lin, J. Functional nanomaterials for near-infrared-triggered cancer therapy. *Biomater. Sci.* **2016,** *4* (6), 890-909.

[12] Zhang, Y.; Shen, T.; Deng, X.; Ma, Y.; Wang, L.; Peng, Y.; Wu, J.; Zhang, Z.; Liu, W.; Tang, Y. Design of a versatile nanocomposite for 'seeing' drug release and action behavior. *J. Mater. Chem. B* **2015,** *3* (43), 8449-8458.

[13] Wu, S.; Huang, X.; Du, X. pH- and redox-triggered synergistic controlled release of a ZnO-gated hollow mesoporous silica drug delivery system. *J. Mater. Chem. B* **2015,** *3* (7), 1426-1432.

[14] Yan, B.; Boyer, J. C.; Branda, N. R.; Zhao, Y. Near-Infrared Light-Triggered Dissociation of Block Copolymer Micelles Using Upconverting Nanoparticles. *J. Am. Chem. Soc.* **2011,** *133* (49), 19714-19717.

[15] Yang, G.; Yang, D.; Yang, P.; Lv, R.; Li, C.; Zhong, C.; He, F.; Gai, S.; Lin, J. A Single 808 nm Near-Infrared Light-Mediated Multiple Imaging and Photodynamic Therapy Based on Titania Coupled Upconversion Nanoparticles. *Chem. Mater.* **2015,** *27* (23), 7957-7968.

[16] Lv, R.; Zhong, C.; Li, R.; Yang, P.; He, F.; Gai, S.; Hou, Z.; Yang, G.; Lin, J. Multifunctional Anticancer Platform for Multimodal Imaging and Visible Light Driven Photodynamic/Photothermal Therapy. *Chem. Mater.* **2015,** *27* (5), 1751-1763.

[17] Yu, M.; Guo, F.; Wang, J.; Tan, F.; Li, N. Photosensitizer-Loaded pH-Responsive Hollow Gold Nanospheres for Single Light-Induced Photothermal/Photodynamic Therapy. *ACS Appl. Mater. Interfaces.* **2015,** *7* (32), 17592-17597.

[18] Zhang, D.; Wu, M.; Zeng, Y.; Wu, L.; Wang, Q.; Han, X.; Liu, X.; Liu, J. Chlorin e6 Conjugated Poly(dopamine) Nanospheres as PDT/PTT Dual-Modal

Therapeutic Agents for Enhanced Cancer Therapy. *ACS Appl. Mater. Interfaces.* **2015,** *7* (15), 8176-8187.

[19] Liu, J.; Detrembleur, C.; De Pauw Gillet, M. C.; Mornet, S.; Jérôme, C.; Duguet, E. Gold Nanorods Coated with Mesoporous Silica Shell as Drug Delivery System for Remote Near Infrared Light ‐ Activated Release and Potential Phototherapy. *Small* **2015,** *11* (19), 2323-2332.

[20] Wang, S.; Huang, P.; Nie, L.; Xing, R.; Liu, D.; Wang, Z.; Lin, J.; Chen, S.; Niu, G.; Lu, G.; Chen, X. Single Continuous Wave Laser Induced Photodynamic/Plasmonic Photothermal Therapy Using Photosensitizer-Functionalized Gold Nanostars. *Adv. Mater.* **2013,** *25* (22), 3055-3061.

[21] Wang, D.; Liu, B.; Quan, Z.; Li, C.; Hou, Z.; Xing, B.; Lin, J. New advances on the marrying of UCNPs and photothermal agents for imaging-guided diagnosis and the therapy of tumors. *J. Mater. Chem. B* **2017,** *5* (12), 2209-2230.

[22] Zhang, Y.; Qian, J.; Wang, D.; Wang, Y.; He, S. Multifunctional Gold Nanorods with Ultrahigh Stability and Tunability for In Vivo Fluorescence Imaging, SERS Detection, and Photodynamic Therapy. *Angew. Chem. Int. Ed.* **2013,** *52* (4), 1148-1151.

[23] Huang, P.; Lin, J.; Wang, S.; Zhou, Z.; Li, Z.; Wang, Z.; Zhang, C.; Yue, X.; Niu, G.; Yang, M.; Cui, D.; Chen, X. Photosensitizer-conjugated silica-coated gold nanoclusters for fluorescence imaging-guided photodynamic therapy. *Biomaterials* **2013,** *34* (19), 4643-4654.

[24] Sun, H.; Sun, X.; Yu, M.; Mishra, A. K.; Huang, L.; Lian, J. Silica-Gold Core-Shell Nanosphere for Ultrafast Dynamic Nanothermometer. *Adv. Funct. Mater.* **2014,** *24* (16), 2389-2395.

[25] Kuo, W. S.; Chang, C. N.; Chang, Y. T.; Yang, M. H.; Chien, Y. H.; Chen, S. J.; Yeh, C. S. Gold nanorods in photodynamic therapy, as hyperthermia agents, and in near-infrared optical imaging. *Angew. Chem.* **2010,** *49* (15), 2711-2715.

[26] Chen, J.; Liang, H.; Lin, L.; Guo, Z.; Sun, P.; Chen, M.; Tian, H.; Deng, M.; Chen, X. Gold-Nanorods-Based Gene Carriers with the Capability of Photoacoustic Imaging and Photothermal Therapy. *ACS Appl. Mater. Interfaces.* **2016,** *8* (46), 31558-31566.

[27] Jang, B.; Park, J. Y.; Tung, C.-H.; Kim, I. H.; Choi, Y. Gold Nanorod−Photosensitizer Complex for Near-Infrared Fluorescence Imaging and Photodynamic/Photothermal Therapy In Vivo. *ACS Nano* **2011,** *5* (2), 1086-1094.

[28] Kaneti, Y. V.; Chen, C.; Liu, M.; Wang, X.; Yang, J. L.; Taylor, R. A.; Jiang, X.; Yu, A. Carbon-Coated Gold Nanorods: A Facile Route to Biocompatible Materials for Photothermal Applications. *ACS Appl. Mater. Interfaces.* **2015,** *7* (46), 25658-25668.

[29] Ma, M.; Chen, H.; Chen, Y.; Wang, X.; Chen, F.; Cui, X.; Shi, J. Au capped magnetic core/mesoporous silica shell nanoparticles for combined photothermo-/chemo-therapy and multimodal imaging. *Biomaterials* **2012,** *33* (3), 989-998.

[30] Nikoobakht, B.; El-Sayed, M. A. Preparation and Growth Mechanism of Gold Nanorods (NRs) Using Seed-Mediated Growth Method. *Chem. Mater.* **2003,** *15* (10), 1957-1962.

[31] Back, T. G.; Moussa, Z. Remarkable Activity of a Novel Cyclic Seleninate Ester as a Glutathione Peroxidase Mimetic and Its Facile in Situ Generation from Allyl 3-Hydroxypropyl Selenide. *J. Am. Chem. Soc.* **2002,** *124* (41), 12104-12105.

[32] Klayman, D. L.; Griffin, T. S. Reaction of selenium with sodium borohydride in protic solvents. A Facile Method for the introduction of selenium into organic molecules. *J. Am. Chem. Soc.* **1973,** *95* (1), 197-199.

[33] Sun, T.; Jin, Y.; Qi, R.; Peng, S.; Fan, B. Post-Assembly of Oxidation-Responsive Amphiphilic Triblock Polymer Containing a Single Diselenide. *Macromol. Chem. Phys.* **2013,** *214* (24), 2875-2881.

[34] Zhang, T.; Ding, Z.; Lin, H.; Cui, L.; Yang, C.; Li, X.; Niu, H.; An, N.; Tong, R.; Qu, F. pH-Sensitive Gold Nanorods with a Mesoporous Silica Shell for Drug Release and Photothermal Therapy. *Eur. J. Inorg. Chem.* **2015,** *2015* (13), 2277-2284.

10.1002/ejic.201800572

TOC

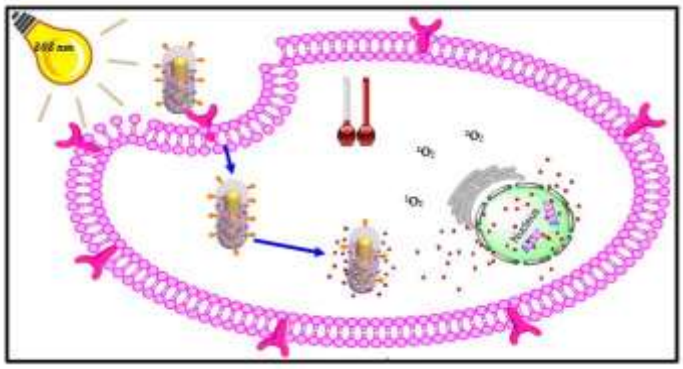

GNRs@mSiO$_2$ core-shell nanoparticles were synthesized as host to load ICG and DOX molecules by layer-by-layer assembly method depending on the electrostatic interaction. Sensitive Se-Se linker was synthesized and grafted outside to insure the controlled release. Under NIR irradiation, the enhanced cytotoxicity to cancer cells is derived from the synergistic effect of chemotherapy, PTT, and PDT.